Reactive mechanism and mechanical properties of in situ composites fabricated from an Al–TiO$_2$ system by friction stir processing

Q. Zhang, B.L. Xiao, W.G. Wang, Z.Y. Ma *

Shenyang National Laboratory for Materials Science, Institute of Metal Research, Chinese Academy of Sciences, 72 Wenhua Road, Shenyang 110016, China

Abstract

In situ (Al$_3$Ti + Al$_2$O$_3$)/Al composites were fabricated from powder mixtures of Al and TiO$_2$ using hot pressing, forging and subsequent multiple-pass friction stir processing (FSP). The reactive mechanism and mechanical properties of the FSPed composites were investigated. Four-pass FSP with 100% overlapping induced the Al–TiO$_2$ reaction, as a result of the enhanced solid diffusion and mechanical activation effect caused by the severe deformation of FSP. Decreasing the size of TiO$_2$ from 450 to 150 nm resulted in the formation of more Al$_3$Ti and Al$_2$O$_3$ particles. The formation mechanisms of Al$_2$O$_3$ and Al$_3$Ti during FSP are understood to be a deformation-assisted interfacial reaction and deformation-assisted solution-precipitation, respectively, based on detailed microstructural observations. The microhardness, Young's modulus and tensile strength of the FSPed composites were substantially enhanced compared with those of FSPed pure Al with the same processing history, and increased as the TiO$_2$ size decreased from 450 to 150 nm. The strengthening mechanisms of the FSPed composites included load transferring, grain refinement and Orowan strengthening, among which Orowan strengthening contributed the most to the yield strength of the composites.
© 2012 Acta Materialia Inc. Published by Elsevier Ltd. All rights reserved.

Keywords: Metal matrix composites; Aluminum; Friction stir processing; Solid-state reaction; Strengthening mechanism

1. Introduction

Chemical reactions between Al and suitable metal oxides, such as CuO [1], Fe$_2$O$_3$ [2] and TiO$_2$ [3,4], have been widely used to produce in situ aluminum matrix composites (AMCs). This process makes use of the fact that the reduction of such oxides by Al results in the formation of another metal and aluminum oxide. The metal can be a good alloying element for the Al matrix, or forms intermetallic phases with Al as the reinforcements. However, the aluminum oxide, especially Al$_2$O$_3$, is a good reinforcement for AMC [5]. Among the reactive systems of Al–metal oxide, the Al–TiO$_2$ system is particularly attractive, since Al$_3$Ti, one of the reactive products, has a relatively low density

(3.4 g cm^{-3}), high Young's modulus (220 GPa) and excellent mechanical properties at both ambient and elevated temperatures [6,7].

Based on these considerations, in situ AMC have been fabricated from an Al–TiO$_2$ system by several in situ techniques, such as reactive hot pressing (RHP) [8], reactive squeeze casting (RSC) [9] and mechanical alloying (MA) [10,11]. The size of Al$_3$Ti in the composites fabricated by RHP and RSC usually grew to >20 μm, owing to the high process temperature [8,9]. The coarse Al$_3$Ti blocks tended to crack under a low stress during tension, resulting in low strength and ductility. The in situ composites fabricated by MA exhibited high strength due to fine Al$_3$Ti particles, but it was always accompanied by significant ductility loss due to contamination introduced by MA [10].

In order to optimize the microstructure and achieve good overall properties of the in situ AMC, the in situ

* Corresponding author. Tel./fax: +86 24 83978908.
  E-mail address: zyma@imr.ac.cn (Z.Y. Ma).

reactive mechanism has been thoroughly investigated. Four main formation mechanisms of in situ particles in AMC are summarized by Tjong and Ma [12], including solution-precipitation, solid–liquid interface reaction, solid–solid interfacial reaction in metal melt and solid diffusion reaction. It is documented that the mechanisms of Al–TiO_2 reaction are dependent on the in situ processing methods. Peng et al. [9] reported that the in situ reaction between Al and TiO_2 during squeeze casting consisted of two steps. First, TiO_2 reacts with molten Al via a solid–liquid interface reaction to form Al_2O_3 particles and Al–Ti solution. Second, during the solidification of Al–Ti solution, Al_3Ti precipitated due to the decreasing solubility of Ti in Al. Barlow et al. [11] and Ying et al. [13] found that the Al–TiO_2 reaction could take place via a solid–solid interfacial reaction, and that mechanical milling facilitated the Al–TiO_2 reaction, owing to the shortened diffusion distance and increased diffusion rate. Furthermore, it was also revealed that some intermediate products such as TiO [4,13] and Ti_2O_3 [14] would be present during the Al–TiO_2 reaction before the final products of Al_2O_3 and Al_3Ti were formed.

Friction stir processing (FSP), a development based on friction stir welding (FSW), is a solid-state processing technique for microstructural modification [15]. During FSP, the material in the processed zone undergoes intense plastic deformation, mixing and thermal exposure, leading to significant microstructural changes. Recently, FSP has been successfully applied to produce in situ intermetallics-reinforced AMC from elemental powder mixtures of Al–Cu [16], Al–Ti [17,18] and Al–Fe [19]. However, the exothermic reactions could not proceed sufficiently even after four-pass FSP with 100% overlapping [16–19].

In a previous study, the in situ AMC was fabricated from an Al–TiO_2 system via hot pressing and subsequent FSP [20]. The preliminary study indicated that the Al–TiO_2 reaction took place in several seconds, forming nano-sized Al_2O_3 and Al_3Ti particles during FSP. Tensile test indicated that the in situ composites exhibited a good combination of strength and ductility. However, the reaction mechanism of Al–TiO_2 during FSP and the strengthening mechanism of the in situ AMC are still not clear.

In this study, two types of TiO_2 particles with sizes of 450 nm and 150 nm were used to fabricate in situ AMC via FSP. The microstructural evolution and mechanical properties were investigated in detail. The aims are to answer the following questions: (1) why the Al–TiO_2 reaction took place in only several seconds during FSP; (2) by which formation mechanisms the in situ reinforcing particles were formed during FSP; and (3) which strengthening mechanisms contributed to the strength of the FSP in situ AMC.

2. Experimental

The starting materials used were commercial pure Al powder (99.9% purity, 13 μm) and rutile TiO_2 powders (99% purity), with average particle sizes of 450 and 150 nm (Fig. 1). The volume fraction of reinforcement ($Al_3Ti + Al_2O_3$) was 25%, assuming that the reaction took place completely to form Al_3Ti and Al_2O_3 (Table 1). The Al and TiO_2 powders were mixed in a bi-axis rotary mixer with a rotation speed of 50 rpm for 12 h. The as-mixed powders were hot-pressed at 823 K and then hot forged at 723 K into disc plates 10 mm thick. The forged plates were subjected to four-pass FSP with 100% overlapping at a tool rotation rate of 1000 rpm and a traverse speed of 25 mm min^{-1}, i.e., four FSP passes were run along the same path. The plates were cooled to room temperature in air between successive passes. A cermet tool with a concave shoulder 20 mm in diameter, a threaded cylindrical pin 6 mm in diameter and 5 mm in length was used. For comparison, an unreinforced pure Al sample was also fabricated and processed under the same conditions. The schematic illustration of FSP is shown in Fig. 2a.

The samples for microstructural investigations were cut in the transverse direction to the FSP. The microstructures were examined by optical microscopy (OM; Zeiss Axiovert 200 MAT), scanning electron microscopy (SEM; Quanta 600) and transmission electron microscopy (TEM; TEC-NAI20) complemented by energy-dispersive spectroscopy (EDS). An X-ray diffraction analyzer (D/max 2400) was used to identify the phases of the composites. The quantitative analysis of XRD results were conducted using Diffrac^{plus} EVA software. The specimen of FSPed pure Al for OM was anodized for 100 s at 0.4 A cm^{-2} in a solution of 5 ml HBF_4 and 200 ml water at room temperature. Thin foils for TEM were prepared by the ion-milling technique.
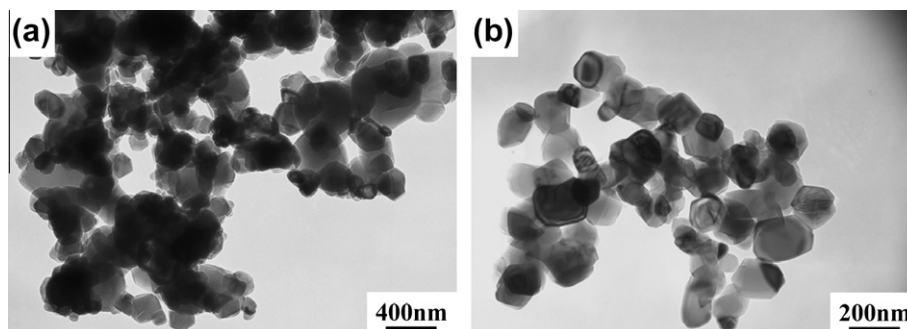

Fig. 1. Morphologies of the TiO_2 powders: (a) 450 nm; (b) 150 nm.

Table 1
Volume fractions of reinforcing particles and elastic moduli of FSPed composites.

	Vol.%		Young's modulus (GPa)
	Al$_3$Ti	α-Al$_2$O$_3$	
Theoretical value[a]	17.2	7.8	
FSPed sample 1	8.7	3.6	85
FSPed sample 2	14.4	5.7	95

[a] Assuming that all the TiO$_2$ reacted with Al to form Al$_3$Ti and α-Al$_2$O$_3$.

Vickers microhardness (HV) measurement was performed on a Leco-LM-247 AT machine along the mid-thickness of the stir zone (SZ) of the FSPed samples by applying a 100 g load for 10 s. The plate specimens (50 × 8 × 2.5 mm) cut in the SZ were subjected to a Young's modulus test on a RFDA HTVP 1750-C machine. Dogbone-shaped tensile specimens (5.0 mm gage length, 1.4 mm gage width and 1.0 mm gage thickness) were electrical discharge machined from the SZ, transverse to the FSP direction, as shown in Fig. 2b. Tensile tests were conducted using an INSTRON 5848 micro-tester at a strain rate of 1×10^{-3} s^{-1}. The property values for each condition were calculated by averaging the three test results. After the tensile test, the fracture surfaces were examined using SEM. The specimens for microstructure investigation and mechanical property test were sampled at least 30 mm away from the FSP start point.

3. Results

3.1. Microstructure

Fig. 3a shows the XRD patterns of the forged samples. For the sample prepared from 450 nm TiO$_2$ (hereafter referred to as sample 1), no evident peaks except for Al and TiO$_2$ peaks were detected, indicating that almost no reaction between Al and TiO$_2$ took place during hot pressing and forging. For the sample prepared from 150 nm TiO$_2$ (hereafter referred to as sample 2), the intensity of TiO$_2$ peaks decreased compared with those in sample 1, whereas the peaks of Al$_3$Ti and α-Al$_2$O$_3$ became evident. Meanwhile, some oxygen-deficient titanium oxides (formulized as Ti$_n$O$_{2n-1}$, such as Ti$_2$O$_3$ and TiO) were revealed. However, insufficient confirmatory peaks were found for definite attribution. These results indicate that a partial reaction between Al and TiO$_2$ took place during hot pressing and forging in sample 2.

Fig. 4a and b shows the microstructures of the forged samples. In both sample 1 and sample 2, initial Al particles
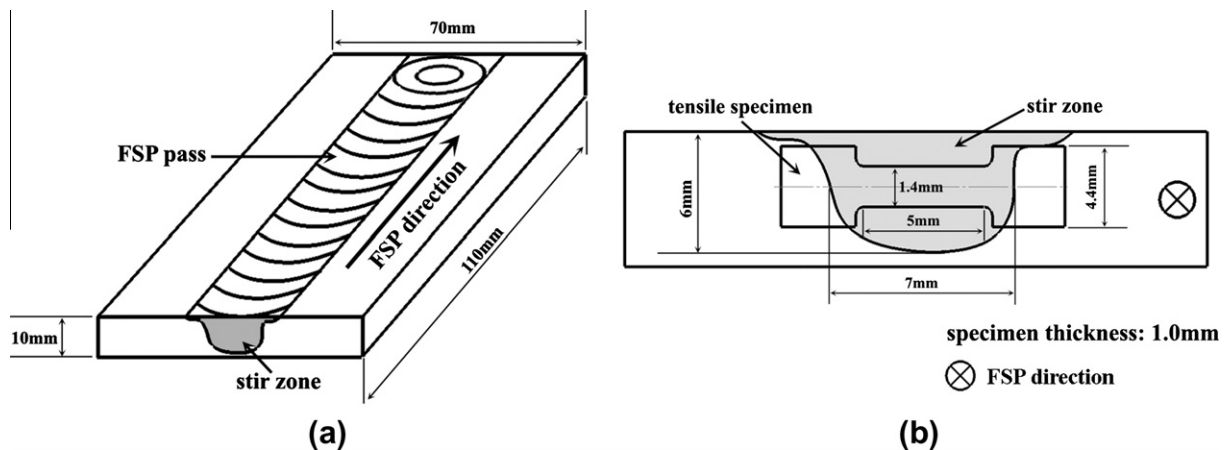

Fig. 2. Schematic illustrations of (a) FSP run and (b) locations of tensile specimens.
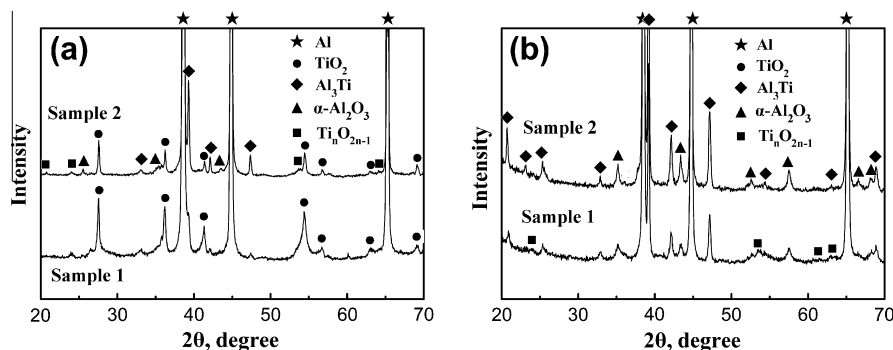

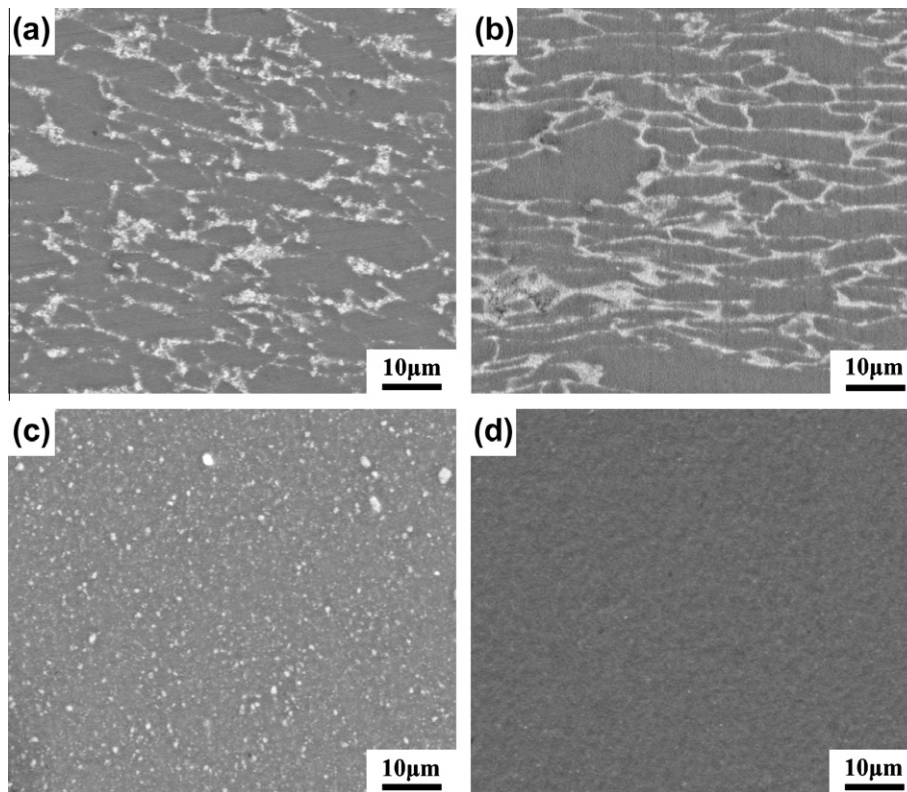Fig. 3. XRD patterns of various composites: (a) as-forged; (b) as-FSPed.

Fig. 4. SEM images of various composites: (a) forged sample 1; (b) forged sample 2; (c) FSPed sample 1; (d) FSPed sample 2.

were elongated by forging. TiO_2 particles were generally distributed at the initial Al particle boundaries, and some particle clusters were observed.

Fig. 3b shows the XRD patterns of the FSPed samples. The peaks corresponding to TiO_2 all disappeared, and some strong peaks corresponding to Al_3Ti and α-Al_2O_3 appeared in the two FSPed samples. Furthermore, some weak peaks corresponding to Ti_nO_{2n-1} were detected in FSPed sample 1. The volume fractions of Al_3Ti and α-Al_2O_3 in the FSPed samples were estimated based on quantitative analysis of the XRD results. As shown in Table 1, the volume fractions of Al_3Ti and α-Al_2O_3 in FSPed sample 2 are more than those in FSPed sample 1, indicating that more reaction took place in FSPed sample 2. However, the volume fractions of Al_3Ti and α-Al_2O_3 in FSPed sample 2 are still lower than the theoretical values, assuming that all TiO_2 particles react with Al to form Al_3Ti and α-Al_2O_3 (Table 1). This indicates that there are still some oxygen-deficient titanium oxides in FSPed sample 2, though no evident peaks corresponding to these phases were detected in the XRD pattern, because of either insufficient concentration or too small a crystallite size [21].

Fig. 4c and d shows that the initial Al particle boundaries in the FSPed samples disappeared. In FSPed sample 1, the in situ formed particles were distributed homogeneously in the Al matrix, whereas in FSPed sample 2 the particles were too fine to be resolved under SEM. TEM and OM observations indicated that the grains in both FSPed pure Al and the composites were equiaxed

(Fig. 5). The FSPed pure Al had an average grain size of $\sim$8.3 μm (Fig. 5c); by comparison, the grain sizes in FSPed samples 1 and 2 were refined to 1.3 and 1.2 μm, respectively (Fig. 5a and b). The grain size distributions of the two FSPed samples are shown in Fig. 6a and b.

Fig. 5a and b shows that nano-sized particles were randomly distributed both within the grain interiors and at the grain boundaries for both FSPed samples. Fig. 7 shows that the particles in the FSPed samples had two different shapes. One is equiaxed, and the other exhibited a floc appearance with an irregular shape. Fig. 6c–f shows the size distributions of the equiaxed and floc-shaped particles in the two FSPed samples. The average sizes of the equiaxed and floc-shaped particles are 85 and 455 nm in FSPed sample 1, and 116 and 204 nm in FSPed sample 2, respectively.

Fig. 8 shows the highly magnified TEM images of FSPed sample 2. The equiaxed particles were identified as Al_3Ti and α-Al_2O_3 by selected electron diffraction patterns (Fig. 8a). Fig. 8b and c shows the HRTEM images of the Al/Al_3Ti and Al/Al_2O_3 interfaces. It is evident from the clear lattice images of Al_3Ti and Al_2O_3 that the matrix Al grains in Fig. 8b and c were not in a zone axis, and hence the atomic fringes in the matrix grains were not visible. The interfaces between the in situ Al_3Ti and α-Al_2O_3 particles and the Al matrix were clean and free from any interfacial phase. Furthermore, no specific orientation relationship was observed between the equiaxed particles and Al matrix.

The magnified image of a floc-shaped particle in FSPed sample 2 is shown in Fig. 9. Some α-Al_2O_3 particles were
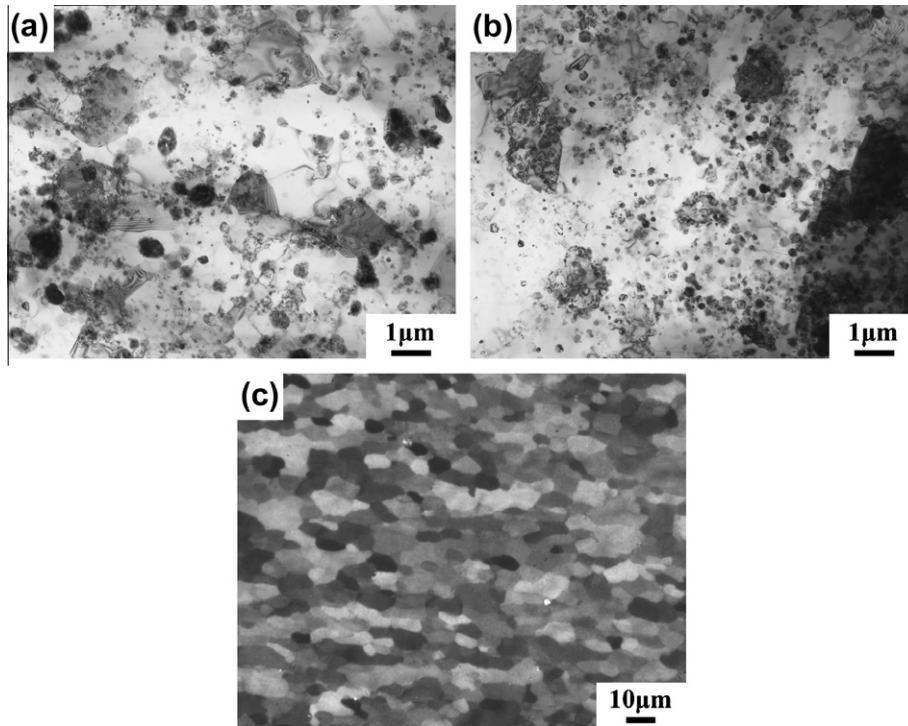
Fig. 5. Grain structures of FSPed samples: (a) sample 1 (TEM); (b) sample 2 (TEM); (c) pure Al (OM).

detected at the boundaries of the floc-shaped particles (Fig. 9a). There is a unique orientation relationship between these α-Al$_2$O$_3$ particles and the Al matrix: $(2\bar{1}\bar{1}3)_{Al_2O_3}||(002)_{Al}$ (Fig. 9b). The clear and symmetrical diffraction patterns cannot be obtained in the floc-shaped particles, probably owing to the complex crystal structures of these particles. EDS analysis indicated that these particles contained Al (40–67 at.%), Ti (11–28 at.%), and O (14–31 at.%) (Fig. 9c).

3.2. Mechanical properties

Fig. 10 shows the hardness profiles of the FSPed composites. The hardness distributions in the SZ of the two FSPed samples are relatively uniform. The average hardness of FSPed sample 1 and sample 2 is 87 HV and 107 HV, respectively. The Young's modulus of FSPed sample 1 and sample 2 is 85 GPa and 95 GPa (Table 1), respectively, which are considerably higher than that of pure Al (70 GPa).

Fig. 11 shows the engineering stress–strain curves of the forged and FSPed samples. The forged samples had the low strength and ductility. In contrast, FSPed sample 1 exhibited a yield strength (YS) of 221 MPa, an ultimate tensile strength (UTS) of 295 MPa, and an elongation of 18.5%. The YS and UTS of FSPed sample 2 were 314 MPa and 415 MPa, respectively, and the elongation was 15.5%. Compared with the FSPed pure Al, the strength increased by ~170% and 280%, respectively, for FSPed samples 1 and 2.

Fig. 12 shows the SEM fractographs of the FSPed samples. FSPed sample 1 showed relatively deep and large dimples on the fracture surface, corresponding to larger elongation, whereas FSPed sample 2 showed shallower and smaller dimples. Furthermore, the size distribution of dimples in FSPed sample 1 was non-uniform, and some large dimples with a size of ~1–2 μm were revealed (white arrows in Fig. 12a), but the large dimples were not observed on the fracture surface of FSPed sample 2 (Fig. 12b).

4. Discussion

4.1. Feasible analysis of Al–TiO$_2$ reaction during FSP

In the present study, XRD results showed that the peaks of TiO$_2$ disappeared and the intense peaks of α-Al$_2$O$_3$ and Al$_3$Ti were revealed in both FSPed samples 1 and 2, indicating that the following reaction took place during FSP:

$$3TiO_2 + 13Al \rightarrow 2\alpha - Al_2O_3 + 3Al_3Ti \tag{1}$$
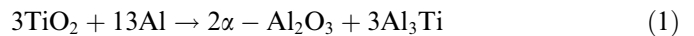
According to the thermodynamic data [22], the relationship between the standard Gibbs free-energy variation (ΔG_T^0) and temperature (T) of reaction (1) can be expressed by:

$$\Delta G_T^0 = -96766.7 + 27.2T \tag{2}$$

According to Eq. (2), the value of ΔG_T^0 would be negative, and reaction (1) can take place spontaneously when the temperature is <3557 K, which is far higher than the temperature in the present investigation. This indicates that reaction (1) has a large thermodynamic driving force.

For Al alloys and AMC, the peak temperature in the SZ during FSW/FSP is usually below the melting point of Al
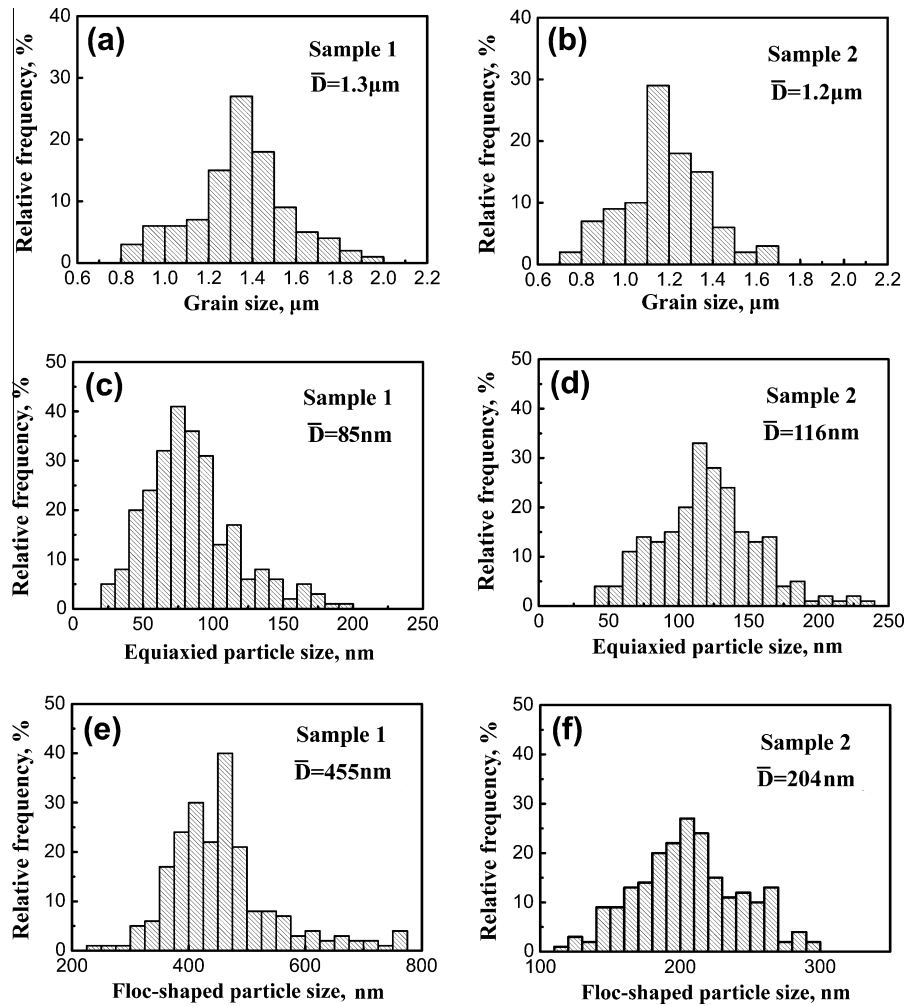
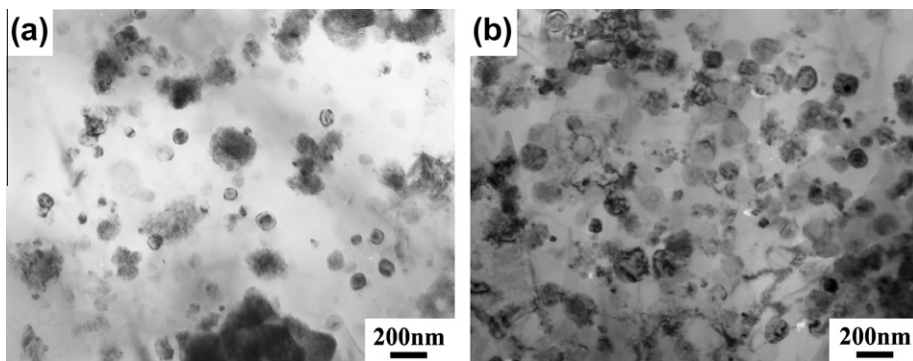Fig. 6. Distributions of grain and particle sizes in FSPed samples.

Fig. 7. Morphologies of particles in FSPed samples: (a) sample 1; (b) sample 2.

[23–25]. In this case, the reaction between Al and TiO_2 is very weak, owing to lower solid-state reaction rates [13,21]. Schaffer and McCormick [26] suggested that the solid-state reaction rate is controlled by diffusion of the reactants through the product materials. The reaction of solids is therefore dependent on the initial contact area, particle size and factors that influence the diffusion rate, such as defect density, local temperature and product morphology. In a thermally activated system, the reactant locations usually remain unchanged and are spatially separated by the reactive products during the course of the reaction, resulting in a lower diffusion rate and then a lower solid-state reaction rate [27].

During FSP, the rotating threaded pin induces severe plastic deformation in the SZ with a strain rate of 10^0–$10^2 \, s^{-1}$ and a strain of up to ~40 [28], resulting in the
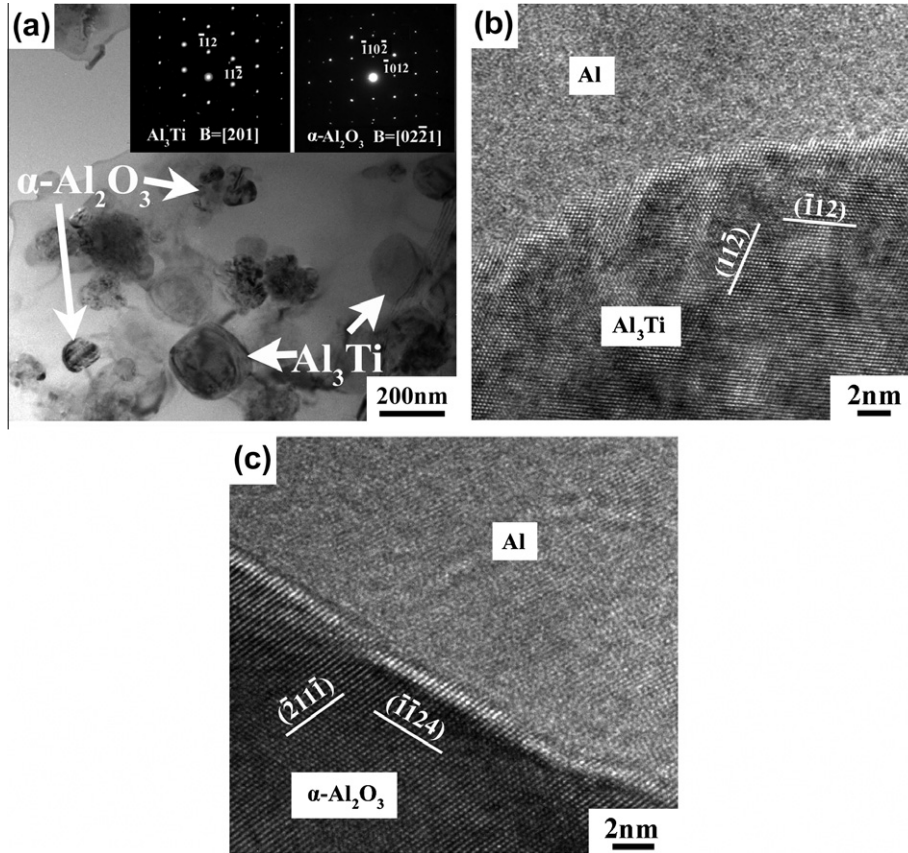
Fig. 8. TEM and HREM images of FSPed sample 2 showing: (a) morphologies of Al₃Ti and α-Al₂O₃; (b) and (c) interfaces of Al₃Ti/Al and Al₂O₃/Al.

breakup of the oxide film surrounding Al and sufficient mixing of Al and TiO_2. In this case, atomically clean surfaces of Al and TiO_2 are brought into intimate contact, facilitating the diffusion between them.

The diffusion flux is directly proportional to the concentration gradients of the diffusion components at the interfaces. For steady-state diffusion, the concentration of components gradually changes at the interfaces, as illustrated in Fig. 13a. The balance of atom concentration would be reached with the occurrence of diffusion. Diffusion during FSP, however, differs from steady-state diffusion, since the balance of atom concentration at the interface between two different components may be destroyed by severe deformation. Consequently, new surfaces with very different compositions meet each other to form new diffusion couples. This situation is depicted in Fig. 13b. Large differences in the atom concentration at the interface therefore promote the diffusion flux through the interface.

Furthermore, a high density of lattice defects, such as dislocations, is introduced by severe plastic deformation during FSP. Then the diffusion will be substantially enhanced owing to the occurrence of pipe diffusion. In contrast, lattice defects probably contribute very little to thermally induced diffusion, because the lattice defects may be annealed out very rapidly at relatively high temperatures [29].

However, based on the theory of reactive kinetics, the molecules or atoms of a reactant should obtain extra energy in order to react with other reactants, though there is enough thermodynamic force to drive the reaction [30]. The extra energy is referred to as activation energy (E_0). The relationship between the reaction rate constant and activation energy can be described by the Arrhenius equation [30]:

$$k = A\exp\left(-\frac{E_0}{RT}\right) \tag{3}$$

where k is the reaction rate constant, T is the reaction temperature, A is a pre-exponential factor, and R is the gas constant. The severe deformation during FSP, which functions like a mechanical activation, may lower the activation energy of reaction and then reduce the reaction temperature and increase the reaction rate.

The mechanical activation during severe deformation can be achieved in the following ways. First, during severe deformation, when dislocations move along a slip plane, the mechanical energy is transformed into the kinetic energy of the atoms, which excites the translational mobility of the atoms [29]. Second, when a solid suffers from stress during mechanical treatment, the structural disorder of the solid is accompanied by chemical bond distorting and bond length extending. If the imposed stress is beyond the chemical bonding energy, the bonds of the solid can be
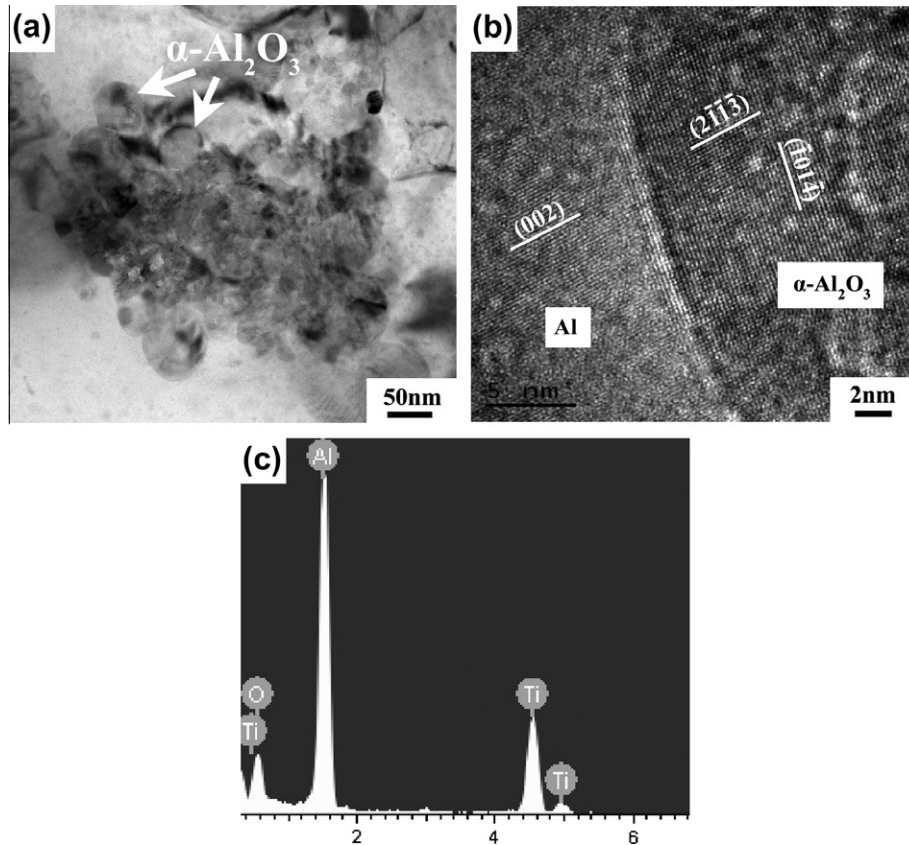
Fig. 9. TEM and HREM images showing (a) morphologies of floc-shaped particles in FSPed sample 2, (b) interface between Al and Al_2O_3 at the boundaries of floc-shaped particles, and (c) EDS results of floc-shaped particles.
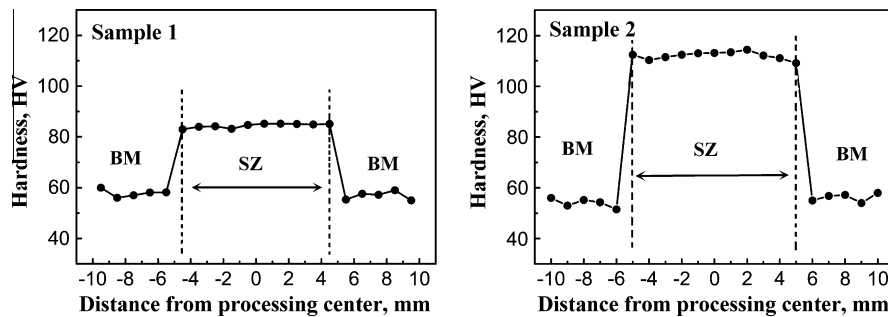

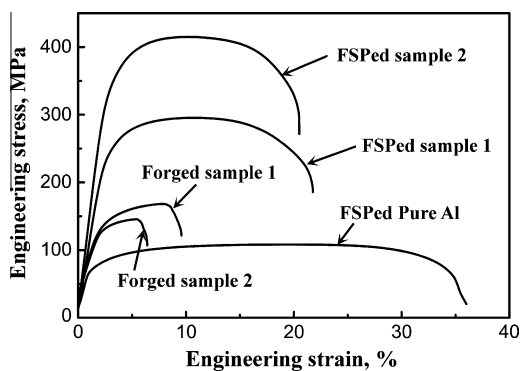Fig. 10. Microhardness profiles of FSPed samples.

Fig. 11. Engineering stress–strain curves of forged and FSPed samples.

effectively broken up, along with the collapse of their crystalline structure. As a result, the molecules or atoms of the reactants are activated and may easily react with other reactants during this process [31]. Third, the grain size decreases dramatically during severe deformation, and the ultra-fine grains decrease the onset temperature of the reaction and enhance the reaction. For example, Wang et al. [32] found that the Fe–Zn reaction in nanostructured Fe (~100 nm) showed an onset temperature decrease of ~21 °C compared with the coarse-grained (CG) sample, and the activation energy for the growth of the Fe–Zn compound layer decreased from ~167.1 kJ mol^{-1} in the CG sample to ~108.0 kJ mol^{-1} in the nanostructured sample.
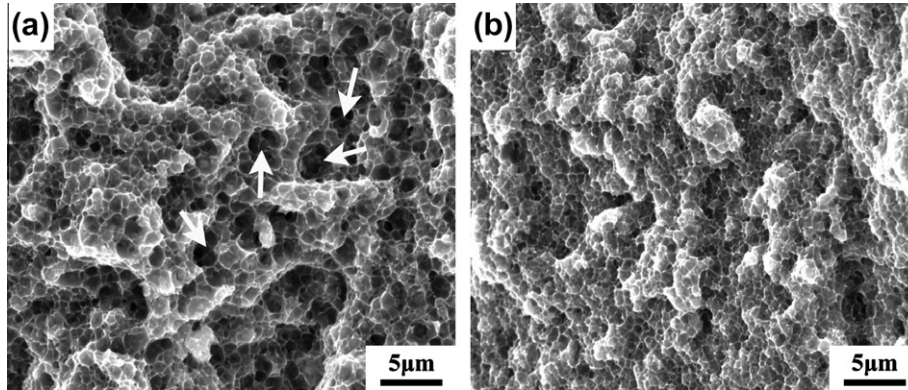
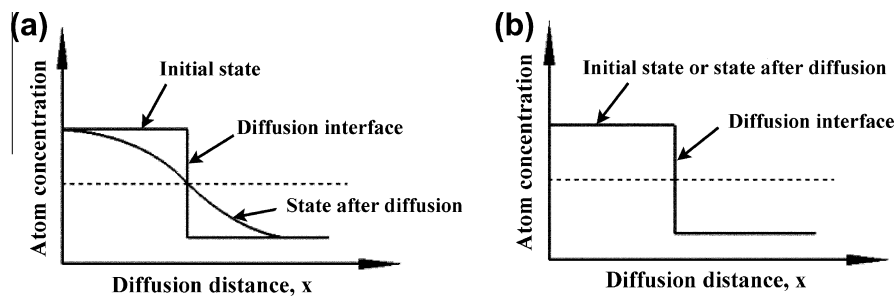Fig. 12. SEM fractographs of FSPed samples: (a) sample 1; (b) sample 2.

Fig. 13. Atom distribution during (a) steady-state diffusion and (b) FSP.

It was reported that newly recrystallized grains around the pin tool during FSP were in the order of 25–100 nm [33,34]. So it is reasonable to expect that the reaction between the ultrafine-grained matrix and TiO_2 will be substantially enhanced during FSP.

Based on above analyses, the occurrence of the Al–TiO_2 reaction during FSP can be attributed to enhanced solid diffusion, which provides sufficient atoms for the Al–TiO_2 reaction, and the mechanical activation effect caused by severe deformation of FSP, which decreases the activation energy of the Al–TiO_2 reaction.

4.2. Formation mechanisms of reinforcements

For other in situ methods, such as RHP and RSC, the in situ reactive process and formation mechanism of reinforcements are usually studied by means of DSC curves and the microstructure of the DSC/DTA samples [4,35,36]. However, for FSP, the in situ reaction takes place under the condition of severe deformation and completes within a very short duration, so the exothermic or endothermic peaks of the DSC curves could not reflect the reaction process during FSP. For example, the DSC curve of the Al–Ti green compact indicated that Al reacted with Ti at ~930 °C, whereas the Al–Ti reaction took place during FSP, though the process temperature was not above 660 °C (melting point of pure Al) [17,18].

The morphology, size and distribution of in situ reinforcement can also shed some light on the reactive mecha-nism. For example, Chu and Premkumar [37] studied the formation mechanism of TiC in an Al–Ti–C system based on the microstructure observation. First, they found that all the TiC particles within the matrix are significantly finer than the original graphite particles used in the mixture. Second, the fine TiC particles are not only round in shape, but also relatively uniform in size. On the basis of these observations, Chu and Premkumar [37] suggested that the in situ formation of TiC is achieved via a mechanism of multiple nucleation and growth from the carbon-satu-rated Al–Ti melt during isothermal holding, i.e., a solu-tion-precipitation mechanism.

4.2.1. Formation mechanism of α-Al_2O_3

The reaction between Al and TiO_2 can be divided into two steps: first, TiO_2 reacts with Al to form α-Al_2O_3 and free Ti atoms, and second, the displaced Ti atoms then react with Al to form Al_3Ti. The reaction formulas are as follows [8]:

$$3TiO_2 + 4Al \rightarrow 2\alpha - Al_2O_3 + 3[Ti] \tag{4}$$

$$[Ti] + 3Al \rightarrow Al_3Ti \tag{5}$$
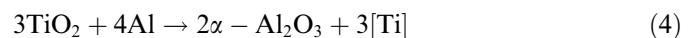
Once reaction (4) has taken place, α-Al_2O_3 particles are formed in situ. However, in this study most of the α-Al_2O_3 particles in the FSPed samples have a size of <100 nm and are smaller than the initial TiO_2 powders, indicating that one TiO_2 particle may transform into several Al_2O_3 particles.
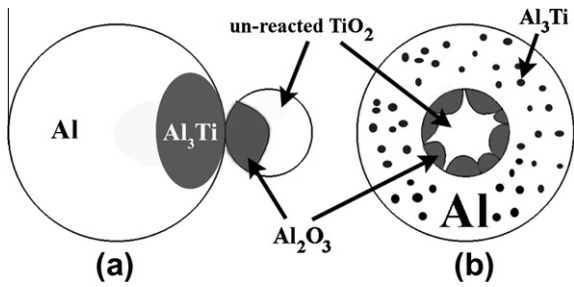
Fig. 14. Schematic diagrams of the formation mechanism of Al$_3$Ti and Al$_2$O$_3$ during (a) hot pressing or sintering and (b) FSP.
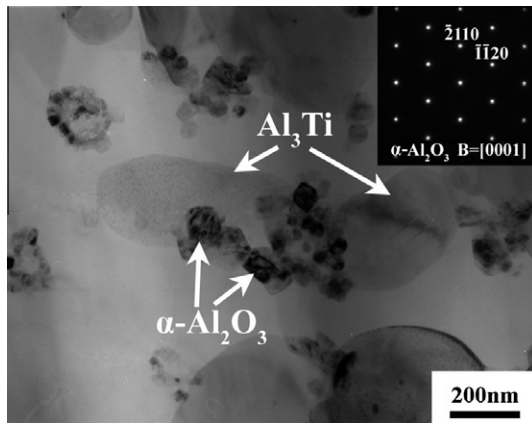

Fig. 15. TEM image of FSPed sample 2 after being heated at 650 °C for 4 h.

Fig. 14 shows a schematic diagram of the formation of reinforcing particles. In the hot-pressed or sintered samples [8,38], TiO$_2$ particles aggregate into the clearance of the initial Al particles. The reaction is controlled by solid-state diffusion at point contacts, and Al$_2$O$_3$ may only be formed at the contact points. As the reaction proceeds, a TiO$_2$ particle gradually transforms into one or two Al$_2$O$_3$ particles from the contact points (Fig. 14a). In this case, the size of Al$_2$O$_3$ is comparable with the size of TiO$_2$.

For the FSPed samples, TiO$_2$ particles were uniformly distributed and surrounded by the Al matrix. The reaction was significantly enhanced by severe deformation of the FSP. In this case, many Al$_2$O$_3$ particles would nucleate and grow on the Al/TiO$_2$ interfaces along the special crystal orientation of the reactant (Fig. 14b). In the present study, an orientation relationship $(2\bar{1}\bar{1}3)_{Al_2O_3}||(002)_{Al}$ was observed between the Al$_2$O$_3$ particles and the Al matrix. In subsequent severe deformation during FSP, most of the Al$_2$O$_3$ particles would become detached from unreacted TiO$_2$ and uniformly distributed in the matrix. And the special orientation relationship between Al$_2$O$_3$ and the matrix would be destroyed.

The results of Feng and Froyen [4,14] suggested that some oxygen-deficient titanium oxides such as Ti$_2$O$_3$ or TiO were formed as intermediate products during the reaction between Al and TiO$_2$ (reaction (4)). Welham [21] also suggested that the removal of oxygen from TiO$_2$ underwent

a sequential process through the oxides of general formula Ti$_n$O$_{2n-1}$ until $n = 1$. In this study, some peaks corresponding to Ti$_n$O$_{2n-1}$ were also detected in FSPed sample 1 (Fig. 3b). Furthermore, some floc-shaped particles containing Al, Ti and O were found in both FSPed samples 1 and 2, and their size was similar to the initial size of TiO$_2$ in both samples. Thus, the floc-shaped particles are considered to be transformed from the initial TiO$_2$ and were the intermediate products of the Al–TiO$_2$ reaction composed of some Ti$_n$O$_{2n-1}$ phases.

In order to verify this viewpoint, FSPed sample 2 was heated at 650 °C for 4 h, and then subjected to TEM examination. It was found that, after heat treatment, the floc-shaped particles transformed into fine α-Al$_2$O$_3$ particles and, at the same time, some coarse Al$_3$Ti particles with a size of 400–600 nm were detected near the α-Al$_2$O$_3$ particles (Fig. 15). This indicates that the floc-shaped particles are the intermediate products of reaction (4) and would react with Al further to form α-Al$_2$O$_3$ and Al$_3$Ti during isothermal holding at 650 °C.

The existence of some intermediate Ti$_n$O$_{2n-1}$ phases suggests that reaction (4) could not proceed completely during FSP, which made the volume fractions of Al$_3$Ti and α-Al$_2$O$_3$ in FSPed samples lower than the theoretical values. Furthermore, no Ti phase was observed in both FSPed samples. These two facts indicate that it was easier for reaction (5) to take place than reaction (4), and the entire Al–TiO$_2$ reaction (reaction (1)) was more likely governed by reaction (4) rather than reaction (5).

Based on the thermodynamics, Gibbs free-energy variation (ΔG_T^0) of reaction (4) was more negative than that of reaction (5) [38]. However, the proceeding of reaction was not only dependent on thermodynamical factors, but also controlled by dynamical factors. The dynamical data of Al–TiO$_2$ reaction would provide some guidance to the Al–TiO$_2$ reaction process. Unfortunately, no dynamical data of Al–TiO$_2$ reaction are available in the previous literature. However, in the Al–ZrO$_2$ system, although the ΔG_T^0 of reaction between Al and ZrO$_2$ to form Al$_2$O$_3$ and Zr is more negative than that between Al and Zr to form Al$_3$Zr, the activation energy of the former reaction is much higher than that of the latter during sintering, indicating that it is much more difficult for the former reaction to take place than the latter [39].

4.2.2. Formation mechanism of Al$_3$Ti

Once reaction (1) has taken place, some free Ti atoms will be formed, according to Eq. (4). Because Ti has low diffusivity and solubility in Al, Al$_3$Ti will form and grow into coarse block-shaped particles at the Al–TiO$_2$ reactive interface in the in situ (Al$_2$O$_3$ + Al$_3$Ti)/Al composites fabricated by RHP [8,38] (illustrated in Fig. 14a). Fig. 7 shows that the Al$_3$Ti particles in the FSPed samples were not only equiaxed in shape, but also relatively uniform in size, and no Al$_3$Ti particles were found at the interface of the floc-shaped particles and Al matrix (Fig. 9a). For FSPed sample 1, the Al$_3$Ti particles were significantly finer than the origi-

nal TiO_2 particles. These microstructural characteristics indicate that the Al_3Ti particles in the FSPed samples might be formed via a solution-precipitation mechanism, like in situ TiB_2 or TiC particles in the Al–Ti–B system [40] or Al–Ti–C system [37].

According to the Al–Ti binary phase diagram, the solubility of Ti in Al is as low as 1.15 wt.% even at 662 °C. However, Kim et al. [41] reported that the solubility of Ti in Al would reach 2.46 wt.% for an Al–20 wt.% Ti sample milled for 15 h. In the present study, severe plastic deformation was induced by four-pass FSP. Biallas et al. [42] suggested that the material flow around the pin during FSP was somewhat similar to the mechanical milling of metal. So it is considered that Ti atoms displaced from TiO_2 (reaction (4)) would first be dissolved into Al. If all the Ti atoms were displaced, the concentration of Ti in Al would reach 8.3 wt.%, which is far greater than the solubility of Ti in Al at solid state. Therefore, as the Al–TiO_2 reaction proceeds, when Ti is supersaturated in Al, the Al_3Ti particles will precipitate. The precipitation of Al_3Ti reduces the supersaturation degree and then promotes the solution of Ti in Al in turn. This cycle proceeds until no more Ti atoms are displaced from TiO_2.

The nano-sized Al_3Ti particles, with a narrow size distribution, indicate that the nucleation of Al_3Ti is easier than the growth. First, the high solubility of Ti in Al caused by severe plastic deformation during FSP increases the degree of supersaturation, and increases the driving force of nucleation. Second, the high density of dislocations produced by severe plastic deformation not only provided nucleation sites of Al_3Ti, but also assisted in the growth of an embryo beyond the critical size by providing a diffusion pipe [11,43,44]. Third, the duration of FSP was very short, and the peak temperature was relatively low compared with other in situ processing methods [12], thus the coarsening of Al_3Ti was restrained.

Cao and Campbell [45–47] suggested that many intermetallic compounds such as Al_3Ti can nucleate on oxides such as MgO or α-Al_2O_3. Nucleation on these oxides would reduce the nucleation energy because of the low planar disregistry of the crystal structures between these intermetallic compounds and oxides during the solidification of Al alloys. In the present study, almost no Al_3Ti growing on Al_2O_3 particles were observed, indicating that nucleation of Al_3Ti on Al_2O_3 may not be the dominant mechanism of Al_3Ti precipitation. As mentioned above, the high density of dislocations can be produced during FSP. Nucleation on the dislocations can also reduce the nucleation energy, and rapid pipe diffusion through dislocations would facilitate the growth of crystal nuclei [11,43,44]. These two factors may result in the nucleation and growth of Al_3Ti on the dislocations being much easier than that on the Al_2O_3 particles during FSP.

It was reported that Al_3Ti particles could act as active nuclei for Al grains during solidification, because Al_3Ti is usually observed at the center of Al grains, and there is a well-established orientation between the lattices of the two phases [48]. In this study, no specific orientation relationship was observed between the equiaxed Al_3Ti particles and Al matrix, indicating that the Al grains might not nucleate on Al_3Ti particles during recrystallization of FSP in solid state.

The driving force of recrystallization is stored deformation energy, and thus only large particles (>1 μm) may act as nucleation sites for recrystallization, because the large particles would cause heterogeneity of deformation in the matrix and a severe deformation zone in the vicinity of the particles [49]. In the present study, the Al_3Ti or Al_2O_3 particles are much smaller than 1 μm in size, so they would not act as the nucleation sites for recrystallization, thus no specific orientation relationship was observed between the equiaxed Al_3Ti or Al_2O_3 particles and Al matrix. However, these fine particles may exert a significant pinning effect on Al grain boundaries and hinder the growth of recrystallized Al grains [49].

As shown in Fig. 6, the size of A_3Ti particles in FSPed sample 2 was coarser than that in FSPed sample 1, though the original TiO_2 used in sample 2 was finer than that in sample 1. This can be explained as follows. First, the original TiO_2 used in sample 2 would be more active than that in sample 1 owing to the smaller particle size. Thus, a partial reaction had taken place to form some Al_3Ti during hot pressing and forging. These particles were coarsened slightly during FSP. Second, the results of XRD showed that more Al_3O_2 were formed in FSPed sample 2, indicating that more free Ti atoms were formed according to Eq. (4). The high concentration of free Ti atoms would facilitate the growth of Al_3Ti particles.

4.3. Mechanical properties

Fig. 10 shows that the HV hardness values in both FSPed samples 1 and 2 were relatively uniform throughout the whole SZ, indicating that the SZ were basically symmetric and uniform. Generally, an onion ring structure, which has been explained by variations in grain size [50], particle-rich band [51] or texture [52], may form in the SZ of single-pass FSPed samples, and this caused a hardness fluctuation in the SZ. In this study, four-pass FSP with 100% overlapping caused more severe deformation and more thorough mixing of the particles and matrix, resulting in a uniform microstructure and hardness distribution in the SZ. Furthermore, the average hardness increased from 85 to 107 HV, with a decrease in the size of TiO_2 from 450 to 150 nm. This can be attributed to the fact that more reinforcements were formed in FSPed sample 2, resulting in a greater strengthening effect. The strengthening mechanisms of the FSPed samples will be discussed in detail later.

The Young's modulus of FSPed sample 1 and sample 2 is 85 and 95 GPa, respectively, which is considerably higher than that of aluminum (70 GPa). This can be attributed to the presence of a large amount of reinforcing particles (Al_3Ti and Al_2O_3) and good interfacial bonding for effective load transfer. The modulus of FSPed sample 2 is

Table 2
Contributions of each strengthening mechanism to the strength of FSPed composites.

	σ_u (MPa)	σ_g (MPa)	σ_{OR} (MPa)	σ_{my} (MPa)	σ_{cy} (MPa)	Experimental YS (MPa)
FSPed sample 1	69	38	98	205	215	221
FSPed sample 2	69	42	126	237	261	314

higher than that of FSPed sample 1 because of more reinforcing particles in FSPed sample 2 (Table 1).

The forged samples exhibited low strength and ductility because of inhomogeneous distribution and a relatively small number of reinforcing particles (Figs. 3 and 4). Four-pass FSP resulted in significant improvements in both strength and ductility. Compared with FSPed pure Al processed with the same parameters, the YS of FSPed sample 1 and sample 2 increased by 152 MPa and 245 MPa, respectively.

The strengthening mechanisms that may operate in particle-reinforced AMC have been considered in several publications. In general, two approaches have been used to account for the strength in particle reinforced AMC. One is based on the load transferring effect (the continuum mechanics) and the other is based on the influence of particles on dislocation movement (micromechanics strengthening) [53]. The YS of composites could also be predicted by incorporating both approaches [54].

By considering the load transferring effect of reinforcing particles, the YS of composites (σ_{cy}) can be expressed as [55]

$$\sigma_{cy} = \sigma_{my}[V_f(s+2)/2 + (1 - V_f)] \quad (6)$$

where σ_{my} is the YS of the matrix, V_f is the volume fraction of the reinforcing particles, and s is the aspect ratio of the reinforcing particles, which is 1 for equiaxed particles.

Considering the contribution of the micromechanics strengthening resulting from the reinforcing particles, including Orowan strengthening (σ_{OR}), grain refinement strengthening (σ_g) and quench strengthening due to the dislocations generated by CTE (coefficient of thermal expansion) mismatch (σ_{CTE}), the YS of the matrix can be expressed as [53]

$$\sigma_{my} = \sigma_u + \sigma_{OR} + \sigma_g + \sigma_{CTE} \quad (7)$$

where σ_u is the strength of the unreinforced matrix.

Previous studies [56,57] suggested that the contribution of quench strengthening can be neglected in the AMC reinforced by submicron particles. The strength increment caused by grain refinement can be expressed by the Hall–Petch relationship:

$$\sigma_g = \sigma_0 + kd^{-1/2} \quad (8)$$

where σ_0 is rationalized as either a frictional stress to the motion of dislocation glide or an internal back stress, d is the matrix grain size in the composites, and k is the Hall–Petch slope, which is ~74 MPa $\mu m^{1/2}$ for pure Al [58].

To calculate the contribution of Orowan strengthening by Al_3Ti and Al_2O_3 particles, it is assumed that all Al_3Ti

and Al_2O_3 particles are spherical and uniformly distributed. The interparticle spacing λ can be calculated by [59]

$$\lambda = \sqrt{2/3}\left[1.25\sqrt{\pi/V} - 2\right]r \quad (9)$$

where r is the average radius of the particles. The contribution of the particles to the shear strength can be calculated using the modified Orowan equation given by Martin [59]:

$$\tau_{OR} = \frac{0.81Gb}{2\pi(1-v)^{1/2}\lambda} \ln\left(2\sqrt{2/3}r/r_0\right) \quad (10)$$

where G is the matrix shear modulus, b is the Burgers vector, v is Poisson's ratio, and r_0 is the dislocation core radius. For pure Al, $G = 26.2$ GPa, $b = 0.286$ nm, $v = 0.345$ and $r_0 = 4b$. The relationship between σ_{OR} and τ_{OR} can be expressed as

$$\sigma_{OR} = M\tau_{OR} \quad (11)$$

where M is the Taylor factor, and $M = 3$ for face-centered cubic metals.

The calculated strength from each strengthening mechanism and the experimental values are summarized in Table 2. It indicates that Orowan strengthening contributes the most YS of the composites. The contribution of the load transferring mechanism is relatively small because of the small aspect ratio of particles ($s = 1$) in the FSPed samples. Furthermore, the calculated YS of FSPed sample 1 agrees well with the experimental value, whereas the calculated YS is lower than the experimental value for FSPed sample 2. This can be attributed to the fact that the above calculation neglected the strengthening effect of the floc-shaped particles.

In FSPed sample 1, the average size of floc-shaped particles is ~455 nm, while the grain size is only 1.3 μm. Therefore, the floc-shaped particles are not supposed to interact directly with intragranular dislocations and cannot contribute to the strength via the Orowan mechanism [60]. Because these particles are far larger than the equiaxed Al_3Ti and Al_2O_3 particles, voids would be preferentially formed near or at the interface between these particles and the matrix during tension, resulting in some relatively large dimples on the fracture surfaces (Fig. 11a). For FSPed sample 2, the average size of the floc-shaped particles decreased to ~204 nm, thus the interaction between these particles and the intragranular dislocations cannot be neglected. However, because the volume fraction of the floc-shaped particles is difficult to estimate from the XRD results owing to the weak diffraction peaks of these phases (Fig. 2b), the calculation without considering the strengthening effect of the floc-

shaped particles resulted in the underestimation of the YS for FSPed sample 2.

As shown in Fig. 11 and Table 1, the UTS increment of FSPed sample 1 and sample 2 are 187 and 307 MPa, respectively, compared with FSPed pure Al, which is larger than the calculated total contribution of various strengthening mechanisms. This is attributed to more severe work hardening during tensile testing of FSPed samples caused by reinforcing particles, which contributed some strength to the UTS of FSPed samples [5]. However, as far as the present authors know, no reliable equation or model was established to predict the UTS of dispersion strengthened alloys or composites, because of the complex process of work hardening caused by interaction between particles and dislocations.

5. Conclusions

(1) No reaction and partial reaction took place between Al and TiO_2 with an average size of 450 nm and 150 nm, respectively, during HP and forging. Four-pass FSP induced the Al–TiO_2 reaction, which can be attributed to the enhanced solid diffusion and mechanical activation effect caused by the severe deformation of FSP.

(2) During FSP, Al–TiO_2 reaction produced Al_2O_3 and Ti atoms, then Al_3Ti precipitated from the Al matrix when Ti was supersaturated in Al. Decreasing the size of TiO_2 from 450 to 150 nm resulted in the formation of more Al_3Ti and α-Al_2O_3. The formation mechanisms of Al_2O_3 and Al_3Ti are considered to be deformation-assisted interfacial reaction and deformation-assisted solution-precipitation, respectively.

(3) The microhardness, Young's modulus and tensile strength of the FSPed composites are substantially enhanced compared with those of FSPed pure Al, and increased with a decrease in the TiO_2 size from 450 to 150 nm.

(4) The strengthening mechanisms of the FSPed composites included load transferring, grain refinement and Orowan strengthening, among which Orowan strengthening contributed the most YS of the composites.

Acknowledgements

References

[1] Yu P, Deng CJ, Ma NG, Yau MY, Ng HL. Acta Mater 2003;51:3445.
[2] Roy D, Ghosh S, Basumallick A, Basu B. Mater Sci Eng A 2006;415:202.
[3] Maity PC, Panigrahi SC, Chakraborty PN. Scripta Metall Mater 1993;28:549.
[4] Feng CF, Froyen L. Composite A 2000;31:385.
[5] Lloyd DJ. Int Mater Rev 1994;39:1.
[6] Li TZ, Olevsky EA, Meyers MA. Mater Sci Eng A 2008;473:49.
[7] Wang SH, Kao PW. Acta Mater 1998;46:2675.
[8] Ma ZY, Tjong SC. Metall Mater Trans A 1997;28:1931.
[9] Peng HX, Wang DZ, Geng L, Yao CK. Scripta Mater 1997;37:199.
[10] Kleiner S, Bertocco F, Khalid FA, Beffort O. Mater Chem Phys 2005;89:362.
[11] Barlow IC, Jones H, Rainforth WM. Acta Mater 2001;49:1209.
[12] Tjong SC, Ma ZY. Mater Sci Eng R 2000;29:49.
[13] Ying DY, Zhang DL, Newby M. Metall Mater Trans A 2004;35:2115.
[14] Feng CF, Froyen L. Scripta Mater 1998;39:109.
[15] Mishra RS, Mahoney MW, Mcfadden SX, Mara NA, Mukherjee AK. Scripta Mater 2000;42:163.
[16] Hsu CJ, Kao PW, Ho NJ. Mater Lett 2007;61:1315.
[17] Hsu CJ, Chang CY, Kao PK, Ho NJ, Chang CP. Acta Mater 2006;54:5241.
[18] Zhang Q, Xiao BL, Wang D, Ma ZY. Mater Chem Phys 2011;130:1109.
[19] Lee IS, Kao PW, Ho NJ. Intermetallics 2008;16:1104.
[20] Zhang Q, Xiao BL, Wang QZ, Ma ZY. Mater Lett 2011;65:2070.
[21] Welham NJ. Mater Sci Eng A 1998;255:81.
[22] Barin I. Thermochemical Date of Pure Substances. 3rd ed. Stuttgart: VCH Verlagsgesellschaft; 1995.
[23] Feng AH, Xiao BL, Ma ZY. Compos Sci Technol 2008;68:2141.
[24] Sato YS, Urata M, Kokawa H. Metall Mater Trans A 2002;33:625.
[25] Bozkurt Y, Uzun H, Salman S. J Compos Mater 2011;45:2237.
[26] Schaffer GB, McCormick PG. Metall Trans A 1990;21:2789.
[27] Schaffer GB, McCormick PG. Appl Phys Lett 1989;55:45.
[28] Ma ZY, Pilchak AL, Juhas MC, Williams JC. Scripta Mater 2008;58:361.
[29] Lü L, Lai MO. Mechanical alloying. London: Kluwer Academic Publishers; 1998.
[30] Atkins P, Paula J. Physical chemistry. 8th ed. Oxford: Oxford University Press; 2006.
[31] Zhang W, Zhang X, Liang M, Lu C. Compos Sci Technol 2008;68:2479.
[32] Wang HL, Wang ZB, Lu K. Acta Mater 2012;60:1762.
[33] Rhodes CG, Mahoney MW, Bingel WH, Calabrese M. Scripta Mater 2003;48:1451.
[34] Fonda RW, Bingert JF, Colligan KJ. Scripta Mater 2004;51:243.
[35] Zhang EL, Zeng XC, Zeng SY. Trans Nonferrous Metal Soc China 1996;6:114.
[36] Nukami T, Flemings MC. Metall Mater Trans A 1995;26:1877.
[37] Chu MG, Premkumar MK. Metall Trans A 1993;24:2803.
[38] Zhu HG, Wang HZ, Ge LQ, Xu WJ, Yuan YZ. Mater Sci Eng A 2008;478:87.
[39] Zhu HG, Min J, Li JL, Ai YL, Ge LQ, Wang HZ. Compos Sci Technol 2010;70:2183.
[40] Brinkman HJ, Duazczyk J, Katgerman L. Scripta Mater 1997;37:293.
[41] Kim GH, Kim HS, Kum DW. Scripta Mater 1996;34:421.
[42] Biallas G, Braun R, Donne CD, Staniek G, Keysser WA. In: Proceedings of the 1st international symposium on friction stir welds. Thousand Oaks, CA: TWI; 1999 [cd rom].
[43] Porter DA, Easterling KE. Phase transformation in metal and alloys. 2nd ed. London: Chapman & Hall; 1992.
[44] Shu JQ, Nelson TW, Mishra R, Mahoney M. Acta Mater 2003;51:713.
[45] Cao X, Campbell J. Metall Mater Trans A 2003;34:1409.
[46] Cao X, Campbell J. Metall Mater Trans A 2004;35:1425.
[47] Cao X, Campbell J. Int J Cast Metal Res 2000;13:175.
[48] Campbell J. Castings. 2nd ed. Oxford: Butterworth-Heinemann; 2003.

[49] Humphreys FJ, Hatherly M. Recrystallization and related annealing phenomena. 2nd ed. Amsterdam: Elsevier; 2004.

[50] Schneider JA, Nunes AC. Metall Mater Trans B 2004;35:777.

[51] Sutton MA, Yang B, Reynolds AP, Taylor R. Mater Sci Eng A 2002;323:160.

[52] Xu SW, Deng XM. Acta Mater 2008;26:1326.

[53] Lee IS, Hsu CJ, Chen CF, Ho NJ, Kao PW. Compos Sci Technol 2011;71:693.

[54] Zhang Z, Chen DL. Scripta Mater 2006;54:1321.

[55] Nardone VC, Prewo KM. Scripta Metall 1986;20:43.

[56] Kim CT, Lee JK, Plichta MR. Metall Trans A 1990;21:673.

[57] Lee JK, Earmme YY, Aaronson HI, Russell KC. Metall Trans A 1980;11:1837.

[58] Yu CY, Kao PW, Chang CP. Acta Mater 2005;53:4019.

[59] Martin JW. Micromechanisms in particle hardened alloys. Cambridge: Cambridge University Press; 1980.

[60] Chen CF, Kao PW, Chang LW, Ho NJ. Metal Mater Trans A 2010;41:513.